doi:10.14311/ppt.2025.2.147
Plasma Physics and Technology **12**(2):147–151, 2025

NUMERICAL CHARACTERIZATION OF ARC-INDUCED TURBULENCE IN THE VICINITY OF CURRENT ZERO

M. Buffoni*, B. Galletti

Hitachi Energy Research, Segelhofstrasse 1A, 5405 Baden-Dättwil, Switzerland

* marcelo.buffoni@hitachienergy.com

Abstract. This work presents a numerical investigation of the final physical mechanism responsible for the thermal interruption of the plasma arc in high-voltage circuit breakers, i.e. turbulence, and its interaction with the arc itself in the vicinity of current zero (CZ). In this context, an experiment in which an arc is ignited between two stationary electrode rods, and it is maintained steadily inside a Teflon *de Laval* nozzle by applying a 2 kA constant current is reproduced. The results show that the three-dimensional instabilities observed experimentally to develop in the arc boundary layer around CZ are only a product of the interaction between the hot arc and its surrounding cold flow, and that no magnetic effects nor magnetic-related instabilities are required for turbulence to develop and grow.

Keywords: high-voltage circuit breaker, arc-induced turbulence, current zero, large-eddy simulations.

1. Introduction

When the contacts in a circuit breaker separate, an electric arc is drawn between them. To interrupt the flowing current, the burning arc must be extinguished. This is usually accomplished at a "natural" current zero (CZ) of the alternating current by blowing a highly pressurized gas onto it. Throughout the interruption process the behavior of the arc is characterized by the dominance of the different terms in the energy balance. The arc is heated by Joule effect (ohmic heating) and cooled by radiation, convection, conduction (which includes turbulence mixing). Based on the arcing phase, each of the cooling mechanism becomes relevant.

In the high current phase, the ohmic heat is equilibrated by radiative transport. When the current decreases, the compressed gas flows into the arcing zone and the arc transitions into the axially blown phase. Here radiation and convection dominate the cooling process, while turbulence transport starts to become relevant. When the current is in the close vicinity of (and at) current zero (CZ), the thermal interruption phase is reached and heat removal by turbulent transport becomes dominant at this stage. Convection is almost irrelevant though radiation is still present due to the high gas temperature, i.e., 6000 K.

As the current tends to zero, the arc becomes thinner due to the low current, the vorticity in the mixing layer increases and, eventually, the mixing layer collapses on the arc axis at some distance from the nozzle throat. Therefore, the entire arc becomes unstable and subsequently fully turbulent. As experimentally observed in [1] and then described theoretically in [2] and [3], is this turbulent mixing what significantly augments the cooling of the arc column and leads to the interruption of the conducting path (thermal interruption).

In this work it is shown, through a numerical simulation, that the instabilities leading to a fully turbulent behavior of the arc as the current approaches CZ are due only to the vorticity production caused by the interaction of the hot arc with its surrounding cold flow. Magnetic effects [3] are not responsible for the onset of such instabilities, although they contribute to their growth through the elongation of the arc loops induced by Lorentz force.

In Section 2 the physical model is presented. Section 3 describes the numerical model used for the simulation. In Section 4 the results of the simulation are discussed and presented. Finally, conclusions are provided in Section 5.

2. Physical model

A large-eddy simulation of a plasma arc subject to a strong axial flow is performed. The simulated case is based on the experimental and theoretical investigations carried out by Bötticher et al. [4], Hermann et al. [1, 2, 5] and Ragaller [3]. It corresponds to a typical configuration found in gas blast circuit breakers.

The physical phenomena involved in the evolution of the gas arc-plasma interaction are, to some extent, simplified by assuming that: i) the plasma is considered as continuous fluid, and it is in local chemical and thermodynamic equilibrium (LCE and LTE); ii) magnetic effects as well as external body forces are neglected; iii) charge neutrality holds. The reason why magnetic forces are neglected in this work is discussed in Section 4.

The equations for the large-eddy simulation (LES) are obtained by applying a spatial high-pass filter to the compressible Navier-Stokes equations. This filtering operation cuts off the spatial scales (eddies) that are smaller than the filter width or the grid size of the employed computational mesh. Thus, the resulting equations govern only the dynamics of the

large, grid scale (GS), eddies and the interactions of the small, unresolved (filtered out), eddies on the large ones are "modeled" using subgrid-scale (SGS) models. The filtering operation is defined by

$$\bar{f}(\vec{x},t) = \int_D F\left(\vec{x}-\vec{\xi};\Delta\right) f\left(\vec{\xi},t\right) \mathrm{d}^3\vec{\xi},$$

where $\bar{f}$ represents the filtered flow variable f, D is the three-dimensional domain, $\vec{x}$ and $\vec{\xi}$ are Cartesian vectors and $F\left(\vec{x}-\vec{\xi};\Delta\right)$ is the filter function associated with the cut-off space scale Δ. To avoid SGS terms on the convective terms of the filtered Navier-Stokes equations, it is common for compressible flows to use Favre filtering [6], defined by

$$\widetilde{f} = \frac{\overline{\rho f}}{\bar{\rho}}$$

where the bar denotes large-scale quantities coming from the spatial filtering and the tilde denotes Favre-filtered quantities, and ρ is the density.

Under the above assumptions, and after applying the filtering, the evolving gas-plasma can be described by the following governing equations:

$$\partial_t\bar{\rho} + \partial_k(\bar{\rho}\tilde{u}_k) = 0 \tag{1}$$

$$\partial_t(\bar{\rho}\tilde{u}_k) + \partial_k(\bar{\rho}\tilde{u}_i\tilde{u}_k) + \partial_i\bar{p} - \partial_k\tilde{\epsilon}_{ik} = -\partial_k(\bar{\rho}\tilde{\tau}_{ik}) + \partial_k(\bar{\epsilon}_{ik} - \tilde{\epsilon}_{ik}) \tag{2}$$

$$\partial_t(\bar{\rho}\tilde{H} - \bar{p}) + \partial_k(\bar{\rho}\tilde{H}\tilde{u}_k) + \partial_k(\tilde{q}_k - \tilde{\epsilon}_{ik}\tilde{u}_i) + S_r + Q_o = -\partial_k[\mathcal{Q}_k + \mathcal{J}_k - \mathcal{D}_k - (\bar{q}_k - \tilde{q}_k)] \tag{3}$$

$$\partial_k j_k = 0 \tag{4}$$

$$s_k\partial_k I_\lambda = a\,(I_b - I) \tag{5}$$

together with an equation of state to relate density to pressure and temperature. In the equations above, ∂ is the partial differential operator, t is time, $i,k = 1,2,3$ are the spatial directions, $\tilde{u}$ is the velocity, $\bar{p}$ is the pressure, $\tilde{H} = \tilde{h} + \tilde{u}_i\tilde{u}_i/2$ is the total enthalpy per unit mass, $\tilde{h}$ is the enthalpy per unit mass, $\tilde{\epsilon}$ is the viscous stress tensor, $\tilde{q}_k = -\lambda_c\partial_k\tilde{T}$ is the conduction heat flux, λ_c is the thermal conductivity and $\tilde{T}$ is temperature. The source Q_o represents the heat generated by Joule effect and S_r corresponds to the heat source (or sink) due to radiation.

The equations (1), (2) and (3), correspond to the Favre-filtered compressible Navier-Stokes equations. In them, the terms on the right-hand sides are the SGS terms representing the effects of the unresolved scales on the resolved ones. They contain unfiltered variables and cannot be directly computed. Therefore, to obtain the Navier-Stokes equations in filtered variables only, they require modeling.

In (2), the term $\partial_k(\bar{\epsilon}_{ik} - \tilde{\epsilon}_{ik})$ is usually small when compared to the subgrid stress tensor $(\tilde{\tau}_{ik})$ and, according to Vreman ([7],[8]), is never considered for high Reynolds number flows like the one simulated in this article. Thus, it is here neglected. In (3), four SGS terms arise after filtering: the subgrid heat flux

$$\mathcal{Q}_k = C_p\bar{\rho}\left(\widetilde{u_kT} - \tilde{u}_k\tilde{T}\right),$$

the subgrid viscous diffusion

$$\mathcal{D}_k = \overline{\epsilon_{ik}u_k} - \tilde{\epsilon}_{ik}\tilde{u}_{ik},$$

the subgrid turbulent diffusion

$$\mathcal{J}_k = \frac{1}{2}\bar{\rho}\left(\widetilde{u_ku_iu_i} - \widetilde{u}_k\widetilde{u_iu_i}\right),$$

and $(\bar{q}_k - \tilde{q}_k)$.

The term $(\bar{q}_k - \tilde{q}_k)$, which is created by Favre-filtering the heat flux, is usually accepted to be small compared to the others [7–9] and therefore is in this work neglected. Although models for the diffusion terms, $\mathcal{D}_k$, and $\mathcal{J}_k$ exist in the literature (see i.e., [9]), they are in this work assumed to be small compared to the subgrid heat flux $\mathcal{Q}_k$ and, thus, also neglected.

Taking advantage of the quasi-neutrality assumption, equation (4) represents the electric current conservation, where j_k is the electric current density in the direction k. In this work, the standard Ohm's law $j_k = \sigma E_k$ is used, where σ is the electrical conductivity of the fluid and E_k are the components of the electric field. Since magnetic effects are neglected, it follows that the electric field can be obtained from the electric potential ϕ as $E_k = -\partial_k\phi$, which yields the expression for the electric current conservation to be solved: $\partial_k(\sigma\partial_k\phi) = 0$.

The heat generated by the electric current flowing through the arc plasma (Joule effect) included as a source in the energy equation is $Q_o = j_kj_k/\sigma$.

Finally, the quasi-steady radiative transfer equation (RTE) (5) allows to compute the spectral radiative intensity I_λ for the wavelength λ and in the direction of the unit vector $\hat{\mathbf{s}}$ of components s_k, through a non-scattering medium with absorption coefficient a. The term I_b indicates the spectral radiative intensity for a black body. The RTE is solved according to the spectral integration method reported in [10].

3. Numerical model and simulation

The three-dimensional arc plasma model is developed using a customized functions library implemented within the commercial solver ANSYS® Fluent [11]. The model introduced in the previous section is solved together with the Navier-Stokes equations in a strongly coupled manner. The coupled version of ANSYS® Fluent pressure-based finite volumes solver is used to solve the Favre-filtered compressible Navier-Stokes equations. For the continuity and energy equations, the second-order upwind scheme is used for space discretization and for the momentum equation a bounded central difference is employed [12]. The radiation and the electric current conservation equations are spatially discretized using the first-order upwind scheme and the second-order central difference scheme, respectively. Time advancement of the fully coupled system is performed using the second-order backwards difference scheme.

3.1. Simulation setup

Like in the experiments by Bötticher et al. [4] and Hermann et al. [1], here an arc is ignited between two stationary electrode rods, placed 110 mm apart, and it is maintained by applying a 2 kA constant current. A strong axial flow is created by expanding air at 23 bar from a high-pressure reservoir through a *de Laval* nozzle into atmospheric pressure. After 5 ms, steady state conditions are reached, and the applied current is ramped down to 10 A with a slope of about -40 A/μs corresponding to a current zero slope of a sine wave of about 127 kA peak at 50 Hz (see Figure 1).

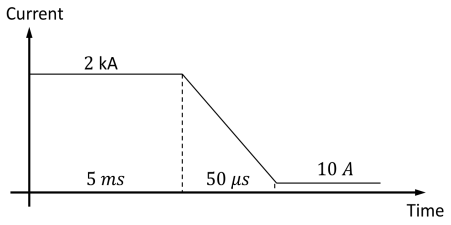

Figure 1. Sketch of the applied current signal.

The geometry of one half of the computational domain employed for the simulation is presented in Figure 2. As shown, one of the electrodes, the anode, is located close to the nozzle exhaust. The other one, the cathode, is placed in the high-pressure part. Both are hollow and shaped internally like nozzles (see Figure 5) so that some gas also flows through them. By doing so, a turbulence-free inflow from the reservoir is guaranteed. Hence, an undisturbed and well-defined laminar region appears in the vicinity of the nozzle inlet having a clear stagnation point.

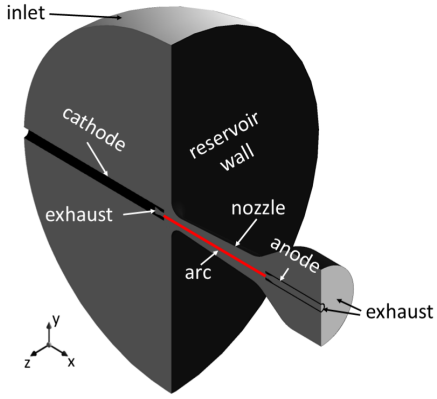

Figure 2. Three-dimensional computational domain with the arc location is also drawn.

The dimensions of the domain correspond, in general, to those of the experimental apparatus in [4]. The distance between the cathode and the nozzle throat is 18 mm. The external diameters of the anode and cathode are, respectively, 8 mm and 10 mm. In both their internal diameter is 4 mm. The nozzle has a length of 76.8 mm, a throat radius of 12 mm, and it is shaped in its diverging part as a cone with a total aperture angle of 8°. The nozzle exhaust radius is 35 mm. To reduce computational effort, instead of being a large tank as in [4], the high-pressure reservoir is modeled as a half sphere of radius 160 mm.

3.2. Computational mesh

A hybrid multi-zone mesh is used for the simulation. It had approximately 3 million cells, and it was generated by blocks. Figure 3 below shows a cut of the computational mesh at a plane with coordinate $z = 0$. What is seen as a "black zone" corresponds to the region of interest for the simulation, that is, the arc and its (close) surrounding area. There, the mesh is particularly refined and, hence, where most of the mesh cells lie. A zoom to that region is presented in Figure 4.

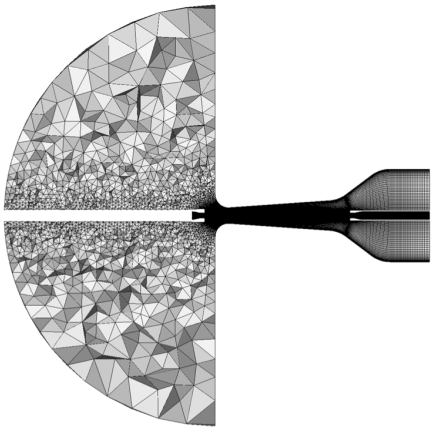

Figure 3. Cut of the computational mesh (plane $z = 0$).

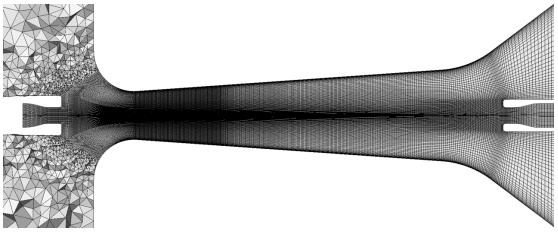

Figure 4. Zoom of the cut of the computational mesh for the region of interest.

Following [4], the nozzle is dimensioned as to provide a layer of cold gas thick enough between the arc boundary layer and the turbulent boundary layer developing at the nozzle wall. To ensure proper resolution of the developing flow mixing layer and the high temperature gradients, a minimum of 27 points are used at the arc plasma/cold gas boundary.

3.3. Boundary and initial conditions

To guarantee constant pressure when (and after) steady state conditions are reached, at the spherical surface of the reservoir a constant total pressure inlet at 23 bar and at 300 K is imposed. The flat part of the half sphere, the boundaries of the electrodes and the boundaries of the nozzle are set as adiabatic, non-slip wall boundaries. At both exhausts, an ambient static pressure of 1 bar is imposed. Except for the initial cylindrical internal parts of the anode and cathode (black zones in Figure 5), where electric current density and zero electric potential are imposed respectively, all the boundaries are set to

zero electric potential flux. All the wall boundaries are treated, independently of the wavelength band, as opaque (all the incident radiation is not transmitted through the boundary wall). Moreover, the radiation energy impacting the opaque walls is only diffusively reflected. The domain is initially at rest, filled with Air at 23 bar and at a temperature of 300 K. The transport and thermodynamic properties, that is, density, thermal conductivity, specific heat, kinematic viscosity, and electrical conductivity, are functions of the local temperature and pressure and are obtained from pre-calculated real-gas look-up tables [13] by the solver during calculation.

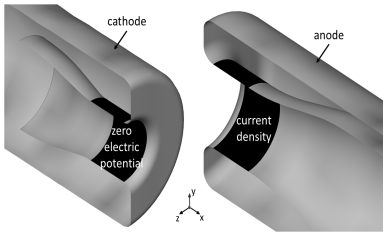

Figure 5. Anode and cathode detail.

In addition, arc attachment at the electrodes is guaranteed throughout the entire simulation by imposing a region of high electrical conductivity defined by volumes having as side surfaces the black zones in Figure 5.

4. Discussion and results

As described in detail in [14], the generation of hydrodynamic turbulence in the boundary layer between a plasma arc and a gas flow can be explained by looking into the terms of the vorticity transport equation, since the necessary condition for turbulence to exist is the presence of vorticity $\vec{\omega}$ in the flow. Keeping in mind the assumptions of Section 2, the standard vorticity transport equation reads

$$\frac{D\vec{\omega}}{Dt} = (\vec{\omega}\cdot\nabla)\,\vec{u} - \vec{\omega}\,(\nabla\cdot\vec{u}) + \nabla\times\left(\frac{\nabla\cdot\vec{\tau}}{\rho}\right) + \nabla p\times\nabla\left(\frac{1}{\rho}\right) \quad (6)$$

The term on the left hand side indicates the material derivative of the vorticity vector. On the right hand side, the first term represents vortex tilting, the second vortex stretching, the third viscous dissipation (where $\vec{\tau}$ is the stress tensor), and the fourth is the baroclinic source of vorticity. Such source term is non-zero whenever a pressure gradient ∇p is not aligned with a density gradient $\nabla\rho$.

In an axially blown arc, the conditions are such that the existence of the vorticity source term is guaranteed. This is a consequence of the flow being subject to both a strong axial pressure gradient due to the expansion in the nozzle and a strong radial density gradient due to the large temperature difference between the arc core and the cold surrounding gas. In this case, given the orientation of the gradients, the vorticity production vector is directed circumferentially (see Figure 6).

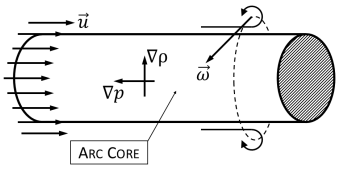

Figure 6. Vorticity production in axially blown arcs.

During the high current phase, the vorticity is confined in a thin mantle at the arc edge (turbulent mixing layer), as illustrated in Figure 7a. As the current tends to zero, the arc gets thinner and the magnitude of the vorticity in the mixing layer increases. Eventually, the mixing layer collapses on the arc axis at some distance from stagnation, resulting in the entire arc becoming first unstable and then fully turbulent, as depicted in Figure 7b.

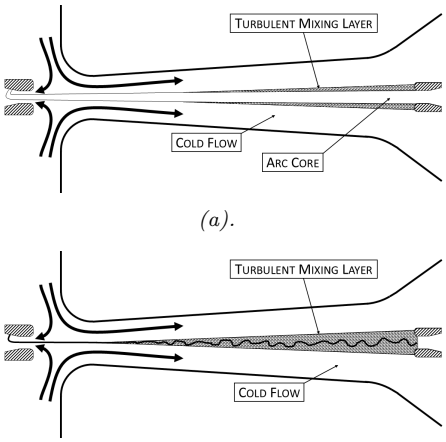

Figure 7. Turbulent mixing layer in an axially blown arc: high (a) and low (b) current phase.

The physical picture described above is confirmed by the findings of the three-dimensional LES-MHD model presented in this work. As shown in Figure 8, in the initial phase, where the current was maintained at 2000 A, the arc column is rotationally symmetric and coaxial with the nozzle axis, while the vorticity exhibits the pattern sketched in Figure 7a.

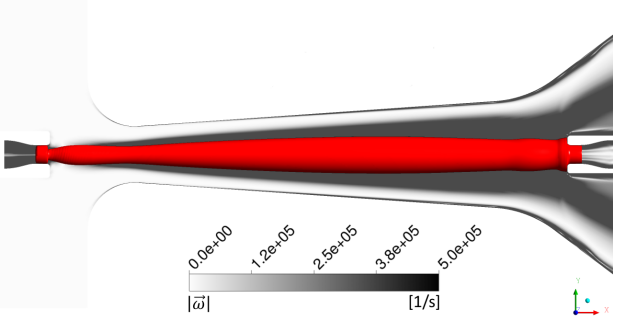

Figure 8. Contours of vorticity magnitude $|\vec{\omega}|$ on the xy-plane together with a 3D iso-surface of the current density magnitude $|\vec{J}|$ at 1.0 A/mm^2 when the current equals 2000 A.

In agreement with the qualitative behavior illustrated in Figure 7b, shortly after the current is ramped

down to 10 A, the arc is destabilized by the vorticity production term at some distance downstream from the stagnation point as shown by Figure 9.

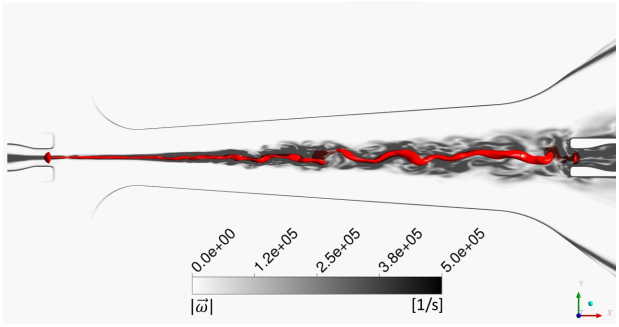

Figure 9. Contours of vorticity magnitude $|\vec{\omega}|$ on the xy-plane together with a 3D iso-surface of the current density magnitude $|\vec{J}|$ at 1.0 A/mm^2 shortly after reaching 10 A.

In light of the above, the choice to exclude magnetic forces from the simulation can be understood. The purpose of this numerical study was indeed to prove that the instabilities observed in the arc shape in the vicinity of CZ are solely due to the vorticity arising from the interaction of the hot arc with the surrounding cold flow. Including Lorentz forces, which is clearly necessary for a consistent numerical representation of arc behavior, has the effect of elongating the loops generated in the arc by the turbulent mixing. This is because the Lorentz force at the tip of the loop, generated by the current flowing in its two sides, acts in a way to stretch the loop itself, regardless of the current orientation. Such stretching mechanism is the same as the one that drives the motion of an arc between two parallel conducting rails [15].

The presented results indicate that the simulated model was able to capture the three-dimensional instabilities observed experimentally in the arc shape at current zero, e.g., [1, 14], demonstrating that they are only caused by the arc-induced turbulence (i.e., by the baroclinic production term of vorticity).

5. Conclusions

This paper considered a large-eddy simulation of a plasma arc subject to a strong axial flow based on the experimental and theoretical studies found in [1–5, 14]. The simulation showed that the three-dimensional instabilities observed experimentally to develop at the arc boundary layer, making the arc unstable and turbulent and leading eventually to current interruption at CZ, are only a product of the arc-induced turbulence caused by the baroclinic generation of vorticity. It was also shown that no magnetic effects [3] are required for turbulence to develop and grow.

References

[1] W. Hermann, U. Kogelschatz, L. Niemeyer, et al. Investigation on the physical phenomena around current zero in HV gas blast breakers. *IEEE Transactions on Power Apparatus and Systems.*, 95(4):1165–1176, 1976. doi:10.1109/T-PAS.1976.32210.

[2] W. Hermann and K. Ragaller. Theoretical description of the current interruption in HV gas blast breakers. *IEEE Transactions on Power Apparatus and Systems.*, 96(5):1546–1555, 1977. doi:10.1109/T-PAS.1977.32483.

[3] K. Ragaller. *Physics of arcs in circuit breakers.* Physical Society of the GDR., 1977.

[4] W. Bötticher, U. Kogelschatz, and E. Schade. Untersuchung quasistationärer Lichtbögen hoher Leistung bei starker axialer Gasströmung. *Zeitschrift für Naturforschung A.*, 27(10):1433–1439, 1972. doi:10.1515/zna-1972-1009.

[5] W. Hermann, U. Kogelschatz, L. Niemeyer, et al. Experimental and theoretical study of a stationary high-current arc in a supersonic nozzle flow. *Journal of Physics D: Applied Physics.*, 7(12):1703–1722, 1974. doi:10.1088/0022-3727/7/12/317.

[6] A. Favre. Turbulence: Space-time statistical properties and behavior in supersonic flows. *Physics of Fluids.*, 26(10):2851–2863, 1983. doi:10.1063/1.864049.

[7] B. Vreman. Direct and large-eddy simulation of the compressible turbulent mixing layer., 1995. PhD-Thesis.

[8] B. Vreman, B. Geurts, and H. Kuerten. Subgrid-modelling in LES of compressible flow. *Applied Scientific Research.*, 54:191–203, 1995. doi:10.1007/BF00849116.

[9] M. Pino Martín, U. Piomelli, and G. Candler. Subgrid-scale models for compressible large-eddy simulations. *Theoretical and Computational Fluid Dynamics.*, 13(5):361–376, 2000. doi:10.1007/PL00020896.

[10] B. Galletti, F. Kassubek, M. Buffoni, et al. Numerical investigation, including experimental validation, of an axially blown, stable arc in argon. *Plasma Physics and Technology*, 6(5):78–81, 2019. doi:10.14311/ppt.2019.1.78.

[11] Ansys® Fluent, Release 2024 R1. ANSYS, Inc.

[12] Ansys® Fluent, Release 2024 R1. *ANSYS Fluent Theory Guide.* ANSYS, Inc.

[13] C. Doiron and K. Hencken. Calculation of thermodynamic and transport properties of thermal plasmas based on the cantera software toolkit., 2014.

[14] L. Niemeyer and K. Ragaller. Development of turbulence by the interaction of gas flow with plasmas., 1972. doi:10.1515/zna-1973-0807.

[15] B. Pafford, J. Sirohi, and L. L. Raja. Propagating-arc magnetohydrodynamic plasma actuator for directional high-authority flow control in atmospheric air. *Journal of Physics D: Applied Physics*, 46(48):485208, 2013. doi:10.1088/0022-3727/46/48/485208.